# Combined experimental and computational study of Ce-doped $La_3Zr_2Li_7O_{12}$ garnet solid state electrolyte

Dong, Bo; Yeandel, Stephen ; Goddard, Pooja; Slater, Peter

*DOI:*
10.1021/acs.chemmater.9b03526



*Document Version*
Publisher's PDF, also known as Version of record

*Citation for published version (Harvard):*
Dong, B, Yeandel, S, Goddard, P & Slater, P 2020, 'Combined experimental and computational study of Ce-doped $La_3Zr_2Li_7O_{12}$ garnet solid state electrolyte', *Chemistry of Materials*, vol. 32, no. 1, pp. 215-223. https://doi.org/10.1021/acs.chemmater.9b03526

CHEMISTRY OF MATERIALS

Article

Cite This: *Chem. Mater.* 2020, 32, 215−223

pubs.acs.org/cm

# Combined Experimental and Computational Study of Ce-Doped $La_3Zr_2Li_7O_{12}$ Garnet Solid-State Electrolyte

Bo Dong,*[,†] Stephen R. Yeandel,[‡] Pooja Goddard,*[,‡] and Peter R. Slater*[,†]

[†]School of Chemistry, University of Birmingham, Birmingham B15 2TT, U.K.

[‡]Department of Chemistry, Loughborough University, Loughborough LE11 3TU, U.K.

Supporting Information

**ABSTRACT:** Li-containing garnet materials have been attracting considerable interest as potential solid-state electrolytes for Li ion batteries. In such $Ln_3M_2Li_xO_{12}$ (Ln = lanthanide, alkaline earth; M = Zr, Hf, Sn, Nb, Ta, Sb, Bi, Te), the best Li ion conductivity is observed for Li contents, $x$, just below the maximum 7.0. The decrease in conductivity for $x$ = 7.0 systems is related to Li ordering (cell changes from cubic to tetragonal) to prevent too short Li−Li interactions. In this work, we report a combined experimental and modeling study of $Ce^{4+}$ doping in $La_3Zr_2Li_7O_{12}$. We show for the first time that $Ce^{4+}$ can be doped onto the $Zr^{4+}$ site in this material. This doping strategy results in a reduction in the tetragonal distortion as well as a lowering of the temperature of the tetragonal−cubic phase transition, attributed to the increase in cell size reducing Li−Li interaction strain. Coupled with these changes, the conductivity shows a significant (1.5 orders of magnitude) improvement. Furthermore, the Ce doping also reduces the interfacial resistance (388 Ω cm$^2$ for $Li_7La_3Z_{1.75}Ce_{0.25}O_{12}$) in contact with Li metal, giving additional potential benefits to this doping strategy. The long-term cycling stability of a Li//garnet//Li symmetric cell over 190 h has been demonstrated.

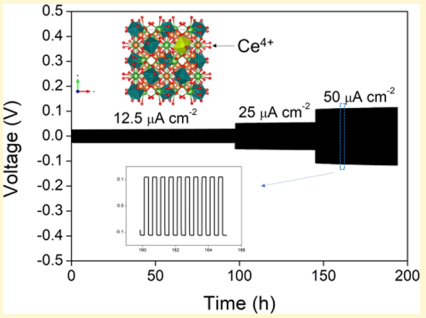


## INTRODUCTION

Lithium ion batteries (LIBs) dominate the energy-storage market for portable electronics and electric vehicles because of their high energy and high power densities and long cycle life.[1,2] However, limitations arising from the organic electrolytes, such as flammability and toxicity, demand the development of next-generation batteries.[3,4] All-solid-state batteries (ASSBs) are seen as ideal candidates to replace traditional lithium ion batteries. ASSBs could operate over a wide electrochemical window and are highly stable at elevated temperatures in ambient atmosphere, thus overcoming safety shortcomings with current LIBs.[5−7]

Since the first report of fast $Li^+$ ion conducting in $La_3M_2Li_5O_{12}$ (M = Nb, Ta), such garnet materials have attracted considerable interest in the last decade.[8,9] The ideal garnet structure has a general formula $A_3B_2C_3O_{12}$, where A, B and C are eight, six, and four oxygen coordinated sites, respectively. In the Li ion conducting garnets, the ability to accommodate extra Li in interstitial sites and the multiple cation sites makes garnets very amenable for structural modification.[10−14] A wide variety of doping strategies have been devised to improve conductivity, including the replacement of A site ions with Ca, Ba, Mg, and Sr; B site ions with Zr, Hf, and Sn; and C site ions with Al and Ga.[15−24] Murugan et al. demonstrated that lithium garnets can accommodate up to seven Li atoms per formula unit reporting cubic $Li_7La_3Zr_2O_{12}$ (LLZO) with high conductivity. However, further studies revealed that $Li_7La_3Zr_2O_{12}$ and related $Li_7La_3(Hf/Sn)_2O_{12}$ system possess tetragonal cells, which are significantly less conductive.[25−27] Structural studies showed that these chemically stoichiometric Li7 tetragonal phases exhibit Li ordering in three fully occupied sites (tetrahedral 8a and octahedral 16f and 32g sites). As the Li content increases toward seven, Li ions are increasingly shifted from the tetrahedral 24d sites to the distorted octahedral 96h sites to avoid short Li−Li repulsive interactions, accounting for the variation of Li ion conductivity and the difference in reported migration pathways.[28,29] Tetragonal to cubic phase transitions have also been shown to be temperature-dependent, with $Li_7La_3Zr_2O_{12}$ and $Li_7La_3Sn_2O_{12}$ transitioning to cubic symmetry above 625−725 °C.[30,31] The observation of cubic "$Li_7La_3Zr_2O_{12}$" at room temperature is attributed to Li loss at the high reaction temperature, long reaction time, and/or from Al exchanging with lithium at the 24d tetrahedral site, due to contamination from the $Al_2O_3$ crucibles.[30,32]

Despite the high electrochemical stability window and mechanical strength in these garnet materials,[33,34] major challenges need to be addressed to enable practical applications; these include: (a) overcoming the large interfacial impedance arising from the rigidity of the garnet electrolyte and poor wettability of Li metal and (b) dendrite growth and expansion through the solid electrolyte.[35] In addition, $H^+/Li^+$ exchange of garnet in humid atmosphere forms LiOH, which reacts with $CO_2$ to form a $Li_2CO_3$ insulating layer.[36−38]

Received: August 29, 2019
Revised: December 11, 2019
Published: December 12, 2019






DOI: 10.1021/acs.chemmater.9b03526
*Chem. Mater.* 2020, 32, 215−223

However, it has been demonstrated that this layer can be effectively removed through mechanical polishing or annealing.[39,40] To overcome the interfacial issue, external pressure or extra heat has been employed to improve the initial physical contact of the cell.[41−43] Interfacial impedance, caused by the microscopic voids and grain boundaries of garnet, can also be negated by coating pellets with metal or nonmetal layers and alloying with Li metal, as shown in this recent review article.[44−47] For example, the formation of a Li-Al-O layer between $Al_2O_3$ and Li has been shown to decrease the interfacial impedance.[48] Hybrid composite garnet−polymer systems combining high ionic conductivity, the good mechanical properties of garnet, and good wetting ability of polymer have also been reported to suppress dendrite nucleation and decrease the interfacial impedance.[49]

As these issues remain unresolved and a highly conductive garnet phase that matches current LIB electrolytes, which is also commercially viable, remains elusive, there is a need to investigate new doping strategies as well as new strategies to minimize interfacial resistance. Ce replacement of La in the formula $Li_{7-x}La_{3-x}Ce_xZr_2O_{12}$ has been reported to stabilize the cubic phase. However, limited Ce incorporation was detected before impurities were observed and no conclusive confirmation of Ce incorporation in the structure was reported.[50]

In this paper, we examine the potential for $Ce^{4+}$ to replace $Zr^{4+}$, the aim being to increase the unit cell size and thus enhance conductivity by reducing the tendency for Li ordering. The corresponding effects on phase transition, conductivity, and electrochemical properties were investigated through a combined experiment and modeling approach, illustrating enhanced performance both in terms of conductivity and interfacial resistance.

## EXPERIMENTAL SECTION

**Synthesis.** $Li_2CO_3$ (99.9%, Alfa Aesar), $LiNO_3$ (99.99%, Sigma-Aldrich), $CeO_2$ (99.9%, Acros), $La_2O_3$ (99.9%, Sigma-Aldrich), and $ZrO_2$ (99%, Sigma-Aldrich) were used as reagents. $Li_2CO_3$ was dried at 180 °C while $La_2O_3$ and $ZrO_2$ were dried at 900 °C before use. $Li_7La_3Zr_{2-x}Ce_xO_{12}$ samples from intimately ground stoichiometric amounts of starting reagents were heated initially to 650 °C for 12 h at a rate of 5 °C $min^{-1}$. Excess $Li_2CO_3$ (15−20%) was added to the mixture to compensate for Li loss during the synthesis. The mixture was then milled ($ZrO_2$ containers and balls) with hexane solvent for 30 min using a Pulverisette 5 planetary ball mill to yield fine powders. The powders were pressed into pellets, placed onto $ZrO_2$ pellets to prevent Al contamination, and reheated at 1000−1050 °C for 12 h in air with a rate of 5 °C $min^{-1}$ to obtain the final product. For future discussion, samples with $x$ = 0, 0.125, and 0.25 are referred to as LLZO, LLZCO125, and LLZCO25, respectively.

**Characterization of Materials.** A Bruker D8 X-ray diffractometer (XRD) with Cu K$\alpha$ radiation and a linear position sensitive detector was used to collect X-ray diffraction data. Patterns were recorded over the 2$\theta$ range of 15−80° with a 0.02° step size. Structural refinement was carried out using the XRD data with the GSAS suite of Rietveld refinement software.[51]

High-temperature XRD data were recorded using a Bruker D8 variable temperature X-ray diffractometer (VTXRD) with a Cu K$\alpha$ radiation and linear-position-sensitive detector. VTXRD data were collected between 25 and 825 °C, with 100 °C interval steps for both heating and cooling processes.

The microstructures of the pellets were assessed by scanning electron microscopy (SEM) using a HITACHI TM4000plus scanning electron microscope. The distribution of elements was probed with an energy-dispersive X-ray (EDX) spectroscopy detector.

For impedance measurements, pellets were pressed and sintered at 1050 °C for 4 h at a rate of 5 °C $min^{-1}$ in dry $N_2$. The pellets were surrounded by the mother powder to decrease the $Li_2O$ loss and avoid reaction with the $Al_2O_3$ crucible. Both sides of the pellet were printed with Au paste and heated at 850 °C for 1 h in air for electrical contact. Alternating current (AC) impedance data were collected with a HP 4192 analyzer with 100 mV applied voltage over the frequency range from 1 to $10^7$ Hz in air.

**Electrochemical Characterization.** Stainless steel (SS) was used as the working electrode and lithium foil, with a thickness of 38 mm, was used as the counter electrode. The SS//$Li_7La_3Zr_{1.75}Ce_{0.25}O_{12}$(LLZCO25)//Li cell was assembled by pressing SS and Li foil on each side of polished LLZCO25 pellet using a Swagelok cell in an argon-filled glove box. The electrochemical stability of SS//LLZCO25//Li cell was tested by cyclic voltammetry (CV) over the voltage range of −0.4 to 4 V vs $Li/Li^+$, with a scan rate of 1 mV $s^{-1}$, using a Biologic SP150 potentiostat. A similar procedure was used for an undoped LLZO pellet for comparison.

To assess interfacial resistance, Li//LLZO//Li and Li//LLZCO25//Li symmetric cells were made by hot pressing Li foils on both sides of polished garnet pellets at 150 °C for 30 min and assembled using Swagelok cells in the argon-filled glove box. Electrochemical impedance spectroscopy (EIS) was conducted using a Solatron 1260 analyzer at 100 mV over the frequency range from 1 to $10^7$ Hz. The plating/stripping curves were recorded using a Bio-logic SP50 cell tester.

**Computational Methodology.** For the computational modeling, the VASP code (version 5.4.4)[52] was employed, which implements a planewave basis-set with projector augmented wave (PAW) pseudopotentials.[53] All calculations were spin-polarized and used the PBEsol functional[54] with an 800 eV planewave energy cutoff. Energy minimization employed a full geometry relaxation including both atomic positions and lattice vectors. The force tolerance for convergence was 0.01 eV $Å^{-1}$ per atom for the geometry optimizations, and the energy tolerance for convergence was $10^{-4}$ eV for the hybrid single point energy calculations.

All LLZO systems were energy minimized in the tetragonal 192 atom unit cell using a converged 2 × 2 × 2 $k$-point grid. The simulation cells used for the bulk oxides comprised the antifluorite structure for $Li_2O$, the baddeleyite structure for $ZrO_2$, and the fluorite structure for $CeO_2$. Both the $\alpha$-$M_2O_3$ and bixbyite-$M_2O_3$ structures were calculated for lanthanum oxide, and the lower-energy polymorph was used for further calculations (the more stable structure was found to be $\alpha$-$La_2O_3$). Metallic lithium was in the body-centered cubic (bcc) lattice. The $k$-point grid was varied until the convergence of energy for each material was reached, and these are given in the Supporting Information (SI) (Table S1).

Energy minimizations were followed by a self-consistent energy calculation using the hybrid HSE06 functional.[55] The parameters were retained as above for $k$-point grid and planewave energy cutoff; however, the Hartree−Fock exchange was calculated on a $k$-point grid half the size.

Defect calculations were performed by inserting a single dopant Ce into the LLZO lattice and then inserting/deleting compensating lithium to maintain charge neutrality if necessary. Compensating lithium interstitial/vacancy was tested as either the nearest neighbor or furthest neighbor to the dopant ion in the periodic system. The substitution of Ce was investigated for the Zr site as well as both La sites.

Redox voltages were calculated by inserting/removing a lithium atom, performing a PBEsol geometry optimization followed by a single point HSE06 calculation. The lattice energy change is then compared to the energy of a lithium atom in metallic lithium, thereby mimicking redox of doped LLZO in a cell with metallic lithium.

## RESULTS AND DISCUSSION

**Phase Formation $La_3Zr_{2-x}Ce_xLi_7O_{12}$.** Stoichiometric $Li_7La_3Zr_2O_{12}$ (LLZO) can be indexed with a tetragonal cell ($I4_1/acd$ space group), while the Ce-doped samples showed a reduction in tetragonal distortion, as shown in Figures 1 and S1. From the determination of the cell parameters, the cell


DOI: 10.1021/acs.chemmater.9b03526
Chem. Mater. 2020, 32, 215−223

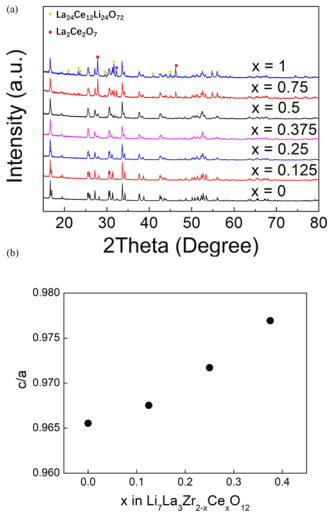


**Figure 1.** (a) XRD patterns of $Li_7La_3Zr_{2-x}Ce_xO_{12}$: $x$ = 0, 0.125, 0.25, 0.375, 0.5, 0.75, 1. (b) Variation of tetragonality ($c/a$) vs composition $x$.

volume was shown to increase linearly as a function of $x$ for $0 \leq x \leq 0.25$ (Figure 2) due to the larger radius of $Ce^{4+}$

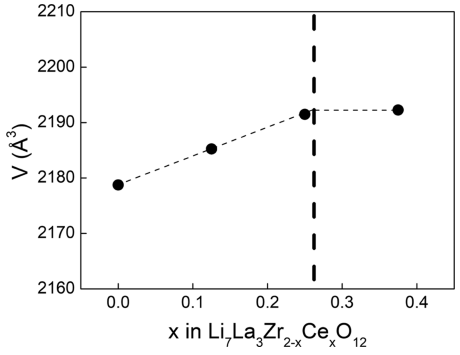


**Figure 2.** Variation of cell volume $V$ of $Li_7La_3Zr_{2-x}Ce_xO_{12}$ with composition $x$.

compared to that of $Zr^{4+}$, indicating the successful replacement of Ce into the LLZO structure (Figure 3). The refined cell volume remained approximately constant when $x > 0.25$, consistent with the detection of the $La_{24}Ce_{12}Li_{24}O_{72}$ (tetragonal, $I4/mmm$ unit cell) impurity phase, which shows that the solid solution limitation resides at $x$ equals ~0.25. With increasing Ce content, $La_2Zr_2O_7$ impurity phase was also detected in the compositions with $x$ = 0.75 and 1. Energy-dispersive X-ray spectroscopy (EDS) mapping results (Figure 4) showed that La, Zr, Ce, and O are uniformly distributed throughout the LLZCO25 sample. From these results, it can therefore be considered that Ce is successfully doped onto the Zr site in the LLZO structure. The relative densities of the sintered pellets are very similar for LLZO (73%) and LLZCO (74%) (SEM images of LLZO and LLZCO25 pellets are shown in Figure S2).

Structure refinement of two compositions, $Li_7La_3Zr_2O_{12}$ and $Li_7La_3Zr_{1.875}Ce_{0.125}O_{12}$, was carried out using XRD data. First, $U_{iso}$ (thermal parameters) of each atom was set to a default value, 0.25 $Å^2$, and the scale factor, background (six terms of shifted Chebyshev function), and lattice parameters were refined. Then, the peak profile coefficient and zero were

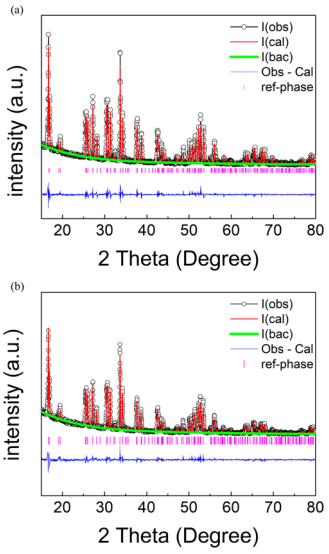


**Figure 3.** Observed, calculated, and difference profiles from the refinement of (a) $Li_7La_3Zr_2O_{12}$ and (b) $Li_7La_3Zr_{1.875}Ce_{0.125}O_{12}$ using XRD data.

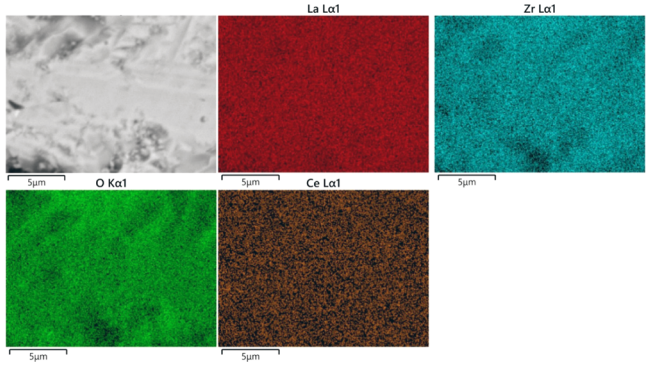


**Figure 4.** EDX elemental mappings of $Li_7La_3Zr_{1.75}Ce_{0.25}O_{12}$.

refined and fixed after convergency. The atomic coordinates of La2, O1, O2, and O3 were refined in turn followed by $U_{iso}$'s of La1, La2, Zr1, O1, O2, and O3. Finally, $U_{iso}$'s of La1, La2, Zr1, O1, O2, and O3 and atomic coordinates of La2, O1, O2, and O3 were refined together. Results for $Li_7La_3Zr_2O_{12}$ are shown in Table 1, which shows full site occupancies for all atoms.

For the refinement of $Li_7La_3Zr_{1.875}Ce_{0.125}O_{12}$, a constraint of the same atomic coordinates and $U_{iso}$'s with overall full site occupancy (Zr1 + Ce1 = 1) was used initially. The scale factor, background, lattice parameters, peak profile coefficient, and zero point were refined in turn. Then, the atomic coordinates of La2, O1, O2, and O3 were refined followed by the occupancies of Zr1/Ce1. Finally, the atomic coordinates of La2, O1, O2, and O3, occupancies of Zr1/Ce1, and $U_{iso}$'s of La1, La2, Zr1, O1, O2, and O3 were refined, giving occupancies of 0.08(2) for Ce1 and 0.92(2) for Zr1. These values correspond to the stoichiometric composition within 2 esds. The final refined parameters of $Li_7La_3Zr_{1.875}Ce_{0.125}O_{12}$ are shown in Table 2.

Further support for the incorporation of Ce on the Zr site is shown in the bond lengths. Selected bond lengths for both $Li_7La_3Zr_2O_{12}$ and $Li_7La_3Zr_{1.875}Ce_{0.125}O_{12}$ are shown in Table 3. As shown in the table, all six Zr1−O1 bonds expand in the Ce-doped sample, which is consistent with the large ionic size of $Ce^{4+}$ to $Zr^{4+}$. The average Zr1/Ce1−O bond length increased


DOI: 10.1021/acs.chemmater.9b03526
Chem. Mater. 2020, 32, 215−223

**Table 1. Refined Structural Parameters of $Li_7La_3Zr_2O_{12}$ Using XRD Data**

| atom | $x$ | $y$ | $z$ | mult. | occupancy | $U_{iso} \times 100$ (Å$^2$) |
|---|---|---|---|---|---|---|
| La1 | 0 | 0.25 | 0.125 | 8 | 1 | 0.2(1) |
| La2 | 0.1271(3) | 0 | 0.25 | 16 | 1 | 0.1(1) |
| Zr1 | 0 | 0 | 0 | 16 | 1 | 0.1(1) |
| O1 | −0.0379(10) | 0.0546(10) | 0.1521(11) | 32 | 1 | 0.8(3) |
| O2 | 0.0540(10) | 0.8503(11) | 0.5379(8) | 32 | 1 | 0.8(3) |
| O3 | 0.1480(11) | 0.0338(10) | 0.4416(9) | 32 | 1 | 0.8(3) |
| Li1 | 0 | 0.25 | 0.375 | 8 | 1 | 2.5 |
| Li2 | 0.1774 | 0.4274 | 0.125 | 16 | 1 | 2.5 |
| Li3 | 0.0800 | 0.0870 | 0.8049 | 32 | 1 | 2.5 |

$a$ = 13.1163(1) Å, $b$ = 13.1163(1) Å, $c$ = 12.6644(2) Å, $V$ = 2178.78(4) Å$^3$
$\chi^2$ = 3.017
$R_{wp}$ = 8.45%, $R_p$ = 7.71%

**Table 2. Refined Structural Parameters of $Li_7La_3Zr_{1.875}Ce_{0.125}O_{12}$ Using XRD Data**

| atom | $x$ | $y$ | $z$ | mult. | occupancy | $U_{iso} \times 100$ (Å$^2$) |
|---|---|---|---|---|---|---|
| La1 | 0 | 0.25 | 0.125 | 8 | 1 | 0.1(1) |
| La2 | 0.1278(3) | 0 | 0.25 | 16 | 1 | 0.3(1) |
| Zr1 | 0 | 0 | 0 | 16 | 0.921(20) | 2.5 |
| Ce1 | 0 | 0 | 0 | 16 | 0.079(20) | 2.5 |
| O1 | −0.0408(13) | 0.0566(13) | 0.1586(13) | 32 | 1 | 2.7(3) |
| O2 | 0.0595(13) | 0.8508(14) | 0.5407(10) | 32 | 1 | 2.7(3) |
| O3 | 0.1494(14) | 0.0387(13) | 0.4394(10) | 32 | 1 | 2.7(3) |
| Li1 | 0 | 0.25 | 0.375 | 8 | 1 | 2.5 |
| Li2 | 0.1774 | 0.4274 | 0.125 | 16 | 1 | 2.5 |
| Li3 | 0.0800 | 0.0870 | 0.8049 | 32 | 1 | 2.5 |

$a$ = 13.1205(2) Å, $b$ = 13.1205(2) Å, $c$ = 12.6940(3) Å, $V$ = 2185.23(7) Å$^3$
$\chi^2$ = 2.863
$R_{wp}$ = 8.62%, $R_p$ = 9.09%

**Table 3. Bond Lengths of Zr1/Ce1−O for $Li_7La_3Zr_2O_{12}$ and $Li_7La_3Zr_{1.875}Ce_{0.125}O_{12}$**

| composition | bond | length (Å) |
|---|---|---|
| $Li_7La_3Zr_2O_{12}$ | Zr1−O1 (2×) | 2.115(14) |
| | Zr1−O2 (2×) | 2.142(14) |
| | Zr1−O3 (2×) | 2.125(14) |
| | average Zr1−O | 2.127(14) |
| $Li_7La_3Zr_{1.875}Ce_{0.125}O_{12}$ | Zr1/Ce1−O1 (2×) | 2.212(18) |
| | Zr1/Ce1−O2 (2×) | 2.171(18) |
| | Zr1/Ce1−O3 (2×) | 2.166(18) |
| | average Zr1/Ce1−O | 2.183(14) |

from 2.127(14) Å for $Li_7La_3Zr_2O_{12}$ to 2.183(14) Å for $Li_7La_3Zr_{1.875}Ce_{0.125}O_{12}$.

VTXRD data of LLZO and LLZCO25 were collected; see Figure 5. The XRD pattern of LLZO showed a tetragonal to cubic phase transition at ∼725 °C, which is consistent with prior work by Larraz et al.[31] LLZCO25, by comparison, shows the transition to the cubic phase at a lower temperature, 325 °C (Figure 5b for LLZCO25). This indicates that the Ce dopant aids in the stabilization of the cubic garnet phase, which is most likely related to the larger size of $Ce^{4+}$ compared to $Zr^{4+}$ (Figure 6).

**Conductivity Results.** A typical impedance dataset for $Li_7La_3Zr_{1.75}Ce_{0.25}O_{12}$ is shown in Figure 7 in three formats. In the complex impedance plane (Figure 7a), a nearly ideal high-frequency semicircle that passes the origin and a low-frequency sharp spike were detected. The corresponding spectroscopic $C'$ plot (Figure 7b) showed a high-frequency plateau with a capacitance of 6.7 pF cm$^{-1}$, with an associated bulk

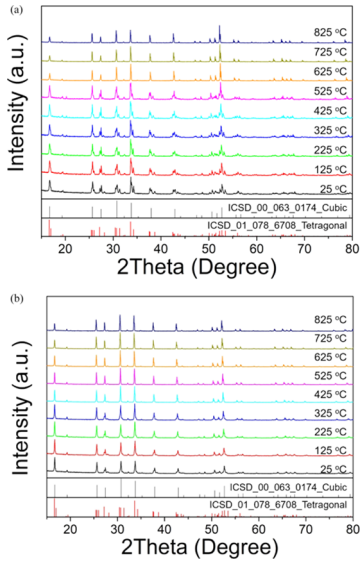


**Figure 5.** Variable temperature XRD of (a) $Li_7La_3Zr_2O_{12}$ and (b) $Li_7La_3Zr_{1.75}Ce_{0.25}O_{12}$ under cooling, showing a tetragonal cell at a low temperature and a cubic cell at a high temperature with the cubic to tetragonal phase transition at ∼725 and 325 °C, respectively.

permittivity of 76.1, as calculated from $\varepsilon_\infty' = C/\varepsilon_0$, where $\varepsilon_0$ is the permittivity of free space with a value of 8.854 × 10$^{-14}$ F cm$^{-1}$.[56] A hypothetical low-frequency plateau with a value of ∼1 μF cm$^{-1}$ at 1 Hz was also observed, which illustrates the ionic blockage at the sample−electrode interface and hence $Li^+$ ion conduction.[57]


DOI: 10.1021/acs.chemmater.9b03526
Chem. Mater. 2020, 32, 215−223

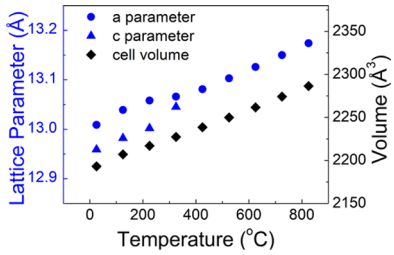


**Figure 6.** Variation in cell parameters vs temperature for $Li_7La_3Zr_{1.75}Ce_{0.25}O_{12}$.

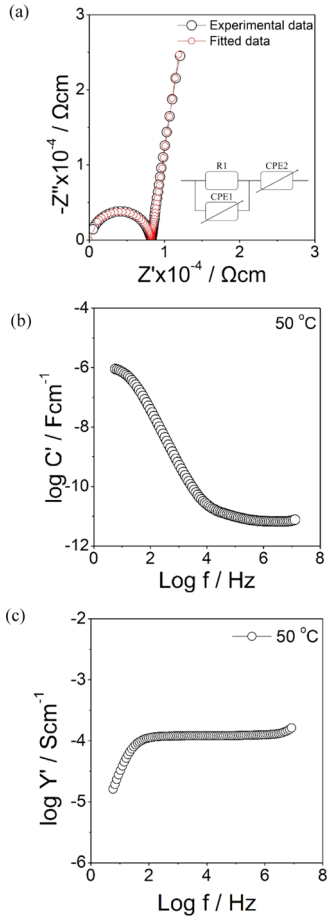


**Figure 7.** (a) Impedance complex plane plot and (b) spectroscopic plots of $C'$ and (c) $Y'$ at 50 °C.

The high-frequency semicircle was fitted with an equivalent circuit using a resistor, $R_1$, and a constant phase element, $CPE_1$, in parallel in the equivalent circuit; see Figure 8a. The CPE is a frequency-dependent resistor and frequency-dependent capacitor in parallel and was used to model the deviation from ideal, Debye-like behavior.[58] Another $CPE_2$ in series with $R_1$ and $CPE_1$ was used to model the low-frequency spike.

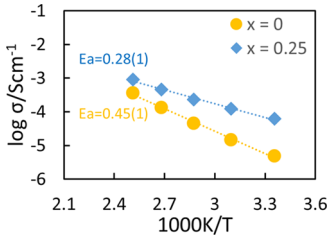


**Figure 8.** Arrhenius plot of $Li_7La_3Zr_{2-x}Ce_xO_{12}$. Activation energies are in eV.

The spectroscopic $Y'$ plot (Figure 7c) shows a frequency-independent plateau at the intermediate frequency, which represents the resistivity of bulk materials, a dispersion at a low frequency that contributed to the double-layer blockage phenomenon at the sample−electrode interface, and curvature at a high frequency associated with the Jonscher's power law.

Bulk conductivity data are shown in Figure 8 for both undoped and Ce-doped $Li_7La_3Zr_2O_{12}$. The conductivity of the Ce-doped ($x$ = 0.25) sample reached $1.2 \times 10^{-4}$ S cm$^{-1}$ at 50 °C with lower activation energy, 0.29 eV, over the temperature range from 50 to 125 °C. The conductivity of this LLZCO25 sample is ∼1.5 orders more than that of LLZO at room temperature (Figure 9).

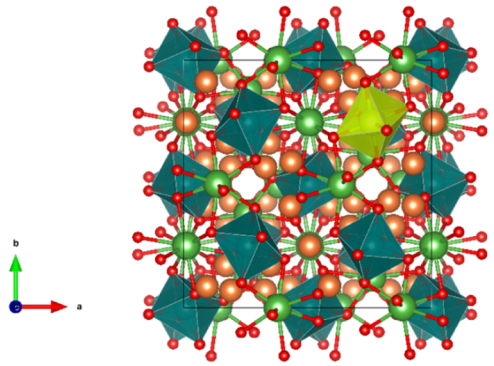


**Figure 9.** $Ce^{4+}$ on the Zr (16c) site. La ions are displayed in green, Zr ion octahedra in teal, Li ions in orange, O ions in red, and the Ce ion octahedra in yellow.

**Modeling.** Doping with $CeO_2$ was investigated for both the La and Zr sites. For doping with $CeO_2$ on the La (16e) site, a charge compensating Li vacancy was introduced

$$La_{La}^{X} + CeO_2 \rightarrow Ce_{La}^{\circ} + v_{Li}' + \frac{1}{2}La_2O_3 + \frac{1}{2}Li_2O$$

This compensating mechanism gives defect energy of 0.90 eV when the two defects in the simulation cell are placed as nearest neighbors and 0.95 eV when placed as far away as possible in the periodic cell. Incorporation on the other La (8b) site gave higher values of 1.12 and 1.35 eV. Incorporation of Ce onto the La site in LLZO has been reported previously by Trofimov et al.;[50,59] however, the samples reported in this work were impure, and the cell parameters showed a cell expansion, which is consistent with Zr rather than La site substitution.

For incorporation of Ce onto the Zr site, no charge compensating defect is required

$$Zr_{Zr}^{X} + CeO_2 \rightarrow Ce_{Zr}^{X} + ZrO_2$$

This mechanism gives a defect energy of 0.98 eV, which is very close to the defect energy of incorporating $Ce^{4+}$ onto the La (16e) site. The similarities in defect energies suggest the potential that $Ce^{4+}$ could be an ambi-site dopant,[60] capable of both La and Zr site substitution. However, experimentally we have only succeeded in attaining single-phase sample $Ce^{4+}$ doping on the $Zr^{4+}$ site. Further compensating mechanisms for $CeO_2$ incorporation are included in the SI.



DOI: 10.1021/acs.chemmater.9b03526
Chem. Mater. 2020, 32, 215−223

Given the experimental evidence of incorporation of Ce onto the Zr site, we have calculated the redox properties of Ce on this site. Redox of $Ce_{Zr}^{X}$ to $Ce_{Zr}'$ is achieved by inserting a lithium ion into the LLZO lattice as either the nearest neighbor or as a furthest neighbor to the dopant ion, giving a range of energies depending on the placement of the interstitial lithium. The $Ce^{4+}$ to $Ce^{3+}$ redox voltage on the Zr site may be calculated via

$$V_{\mathrm{Zr\ site}} = -\frac{E[Li_{57}La_{24}Zr_{15}Ce_1^{3+}O_{96}] - E[Li_{56}La_{24}Zr_{15}Ce_1^{4+}O_{96}] - E[Li_M]}{F}$$

where $E[x]$ is the lattice energy of material $x$ and $F$ is the Faraday constant. When LLZO containing the $Ce_{Zr}^{X}$ species is exposed to lithium metal, the voltage is calculated to be 0.36 V when lithium is inserted as the furthest neighbor and 0.43 V when inserted as the nearest neighbor.

To check whether this result is due to the extra interstitial lithium beyond the usual formula, we have calculated the same value using simulation cells with an additional electron. In this case, the redox is between a −1 charged simulation cell with stoichiometric lithium and a −1 charged cell with a lithium vacancy. The redox voltage is then calculated via

$$V_{\mathrm{Zr\ site}} = -\frac{E[Li_{56}La_{24}Zr_{15}Ce_1^{3+}O_{96}] - E[Li_{55}La_{24}Zr_{15}Ce_1^{4+}O_{96}] - E[Li_M]}{F}$$

This calculation gives a voltage of 1.09 V when lithium is inserted as the furthest neighbor and 0.93 V when lithium is inserted as the nearest neighbor. Both calculated voltages are distinctly different from the voltage calculated when cerium occupies a lanthanum site and undergoes the same redox process, which gives a voltage of approximately 2.37 V (see the SI). This indicates a sensitivity of the voltage to both the doping site and the lithium content when vacant lithium sites are no longer available. Of the different possibilities, the first values (0.36/0.43 V) are consistent with the experimental CV data (see below). This could be explained from the fact that $Ce^{3+}$ is harder to stabilize in the octahedral environment due to the large difference in the ionic radii (1.01 for $Ce^{3+}$ compared to 0.72 for $Zr^{4+}$), and why low potentials, i.e., a strong reductive force, are predicted for doping $Ce^{3+}$ on the octahedral $Zr^{4+}$ site.

The lithium ion diffusion pathways for the cubic phase Ce-doped LLZO would be similar to any other cubic phase of LLZO as the unit cell is so densely packed with Li ions that a different pathway is hard to envisage. Detailed pathways of Li ion in the cubic phase can be found in previous reports using both cation and anion doping strategies.[21,61] As shown in these papers, despite the different doping strategies, the pathways are very similar, and therefore we do not anticipate this to be different when doping with Ce.

**Electrochemical Property.** The electrochemical stabilities of both undoped and Ce-doped samples were tested in SS//LLZO//Li SS//LLZCO25//Li cells by CV from −0.4 to 4 V. As shown in Figure 10, peaks are observed around 0 V for LLZO, which is consistent with Li plating/stripping, as shown in previous studies of such garnet systems. For the LLZCO25 sample, there is a broader peak observed at ∼0.395 V. The broadening of this peak suggests the introduction of an additional feature, which may be attributed to additional cerium redox processes as indicated from the modeling results. The XRD pattern of LLZCO25 after CV measurement showed the partial decomposition of the sample with the formation of a small amount of $Ce_4O_7$ (shown in Figure S3). This may

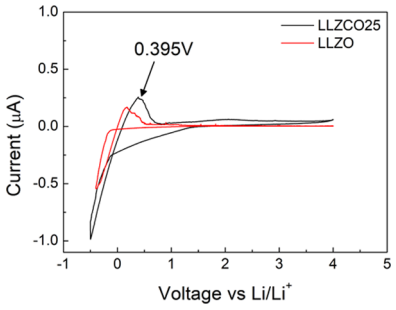


**Figure 10.** CV of $Li_7La_3Zr_2O_{12}$ and $Li_7La_3Zr_{1.75}Ce_{0.25}O_{12}$ with stainless steel and Li metal as working and counter electrodes, at a scanning rate of 1 mV $s^{-1}$.

indicate either the insertion of an extra Li into the garnet structure results in partial decomposition in the region near the Li metal or that there is a simple reaction at the interface between Li and the garnet phase leading to this decomposition product.

The electrochemical impedance spectroscopy (EIS) of symmetric Li cells with LLZO and LLZCO25 pellets shows a significant difference in interfacial resistance at the solid−solid interface (Figure 11). As shown in Figure 11b, the circuit

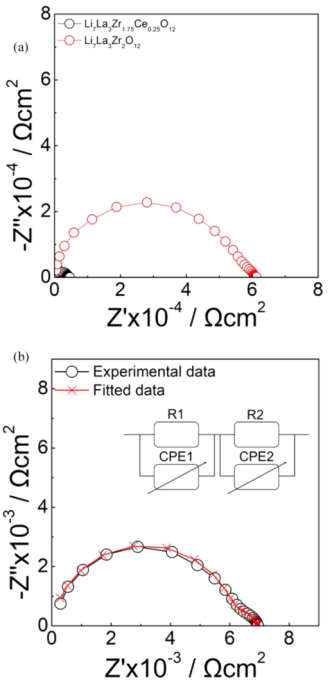


**Figure 11.** (a) Impedance spectra of Li|LLZO|Li and Li|LLZCO25|Li symmetric cells. (b) Impedance spectra of Li|LLZCO25|Li symmetric cell.

of Li//LLZCO25//Li was fitted using two parallel resistors and CPE in series, representing the bulk conductivity and interfacial respondence, respectively. This showed a dramatic decrease in interfacial resistance from 2100 Ω $cm^2$ of Li//LLZO//Li to 388 Ω $cm^2$ of Li//LLZCO25//Li. This enhancement may be associated with the in situ formation of $Ce_4O_7$ interface layer, which has better wettability and higher conductivity. Significantly, this enhancement requires no additional coating as required by prior studies and so suggests that low-level Ce doping in other garnet electrolyte systems,


DOI: 10.1021/acs.chemmater.9b03526
Chem. Mater. 2020, 32, 215−223

e.g., mixed Nb/Zr- or Al/Ga-doped $La_3Zr_2Li_7O_{12}$, should be investigated for potentially reducing interfacial resistances in these highly conducting cubic systems.

The long-term cycling performance of the Li//LLZCO25//Li symmetry cell at 60 °C is shown in Figure 12. A flat voltage

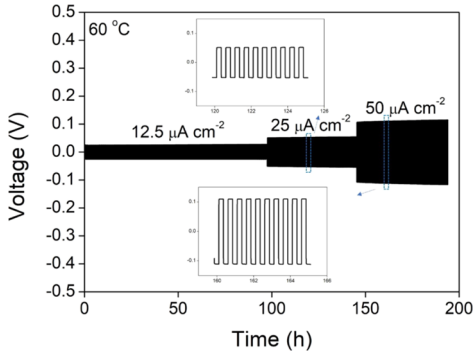


**Figure 12.** Charge−discharge voltage profile of the Li//$Li_7La_3Zr_{1.75}Ce_{0.25}O_{12}$//Li symmetry cell at 60 °C with 12.5, 25, and 50 $\mu$A cm$^{-2}$ current densities.

plateau with a voltage overpotential of 53 mV at 25 $\mu$A cm$^{-2}$ current density was observed. At the current density of 50 $\mu$A cm$^{-2}$, a slightly increasing overpotential is seen; however, the long-term cycling stability over 190 h was still delivered.

## CONCLUSIONS

Cerium doping on the Zr site has been found to be an effective strategy to reduce tetragonal distortion of LLZO, which is most likely related to the larger size of $Ce^{4+}$ than $Zr^{4+}$. VTXRD data show a decrease in the tetragonal−cubic phase transition temperature from 725 °C for LLZO to 325 °C for LLZCO25. Impedance data show enhanced $Li^+$ ion conductivity in the Ce-doped sample with lower activation energy. Both experimental and computational work support the partial reduction of LLZCO25 when contacting with Li metal. This effect most likely accounts for a significant decrease in interfacial resistance (388 Ωcm$^2$) of Ce-doped LLZO, which may be related to the better wettability and higher conductivity of the resultant $Ce_4O_7$ interlayer. These results therefore show an alternative way of reducing the interfacial resistance issue between Li metal and garnet solid-state electrolyte materials, and future studies need to investigate other lightly Ce-doped garnet materials with a view to enhancing the bulk conductivity and hence the overall performance.

## ASSOCIATED CONTENT

### Supporting Information

The Supporting Information is available free of charge at https://pubs.acs.org/doi/10.1021/acs.chemmater.9b03526.

Information on the SEM images of pellets; XRD patterns before and after CV test; DFT parameters, defect formation energies, and redox energies from the calculation (PDF)

Raw data of $Li_7La_3Zr_2O_{12}$, $Li_7La_3Zr_{15}Ce_{05}O_{12}$, $Li_7La_3ZrCeO_{12}$, and CV (XLSX)

## AUTHOR INFORMATION

### Corresponding Authors

*E-mail: b.dong@bham.ac.uk (B.D.).

*E-mail: p.goddard@lboro.ac.uk (P.G.).

*E-mail: p.r.slater@bham.ac.uk(P.R.S.).

### ORCID

Bo Dong: 0000-0003-0964-5852

Stephen R. Yeandel: 0000-0002-6977-1677

Pooja Goddard: 0000-0001-6624-2561

### Notes

The authors declare no competing financial interest.

## ACKNOWLEDGMENTS

P.R.S. and B.D. acknowledge the support of EPSRC grant EP/R024006/1: ICSF Wave 1: GENESIS: Garnet Electrolytes for New Energy Storage Integrated Solutions. P.G. and S.R.Y. acknowledge the support of EPSRC SUPERGEN grant, EP/N001982/1.

## REFERENCES

(1) Goodenough, J. B.; Park, K. S. The Li-Ion Rechargeable Battery: A Perspective. *J. Am. Chem. Soc.* **2013**, *135*, 1167−1176.

(2) Larcher, D.; Tarascon, J. M. Towards Greener and More Sustainable Batteries for Electrical Energy Storage. *Nat. Chem.* **2015**, *7*, 19−29.

(3) Tarascon, J.-M.; Armand, M. Issues and Challenges Facing Rechargeable Lithium Batteries. *Nature* **2001**, *414*, 359−367.

(4) Gadjourova, Z.; Andreev, Y. G.; Tunstall, D. P.; Bruce, P. G. Ionic Conductivity in Crystalline Polymer Electrolytes. *Nature* **2001**, *412*, 520−523.

(5) Janek, J.; Zeier, W. G. A Solid Future for Battery Development. *Nat. Energy* **2016**, *1*, No. 16141.

(6) Bachman, J. C.; Muy, S.; Grimaud, A.; Chang, H. H.; Pour, N.; Lux, S. F.; Paschos, O.; Maglia, F.; Lupart, S.; Lamp, P.; Giordano, L.; Shao-Horn, Y. Inorganic Solid-State Electrolytes for Lithium Batteries: Mechanisms and Properties Governing Ion Conduction. *Chem. Rev.* **2016**, *116*, 140−162.

(7) Ramakumar, S.; Deviannapoorani, C.; Dhivya, L.; Shankar, L. S.; Murugan, R. Lithium Garnets: Synthesis, Structure, $Li^+$ Conductivity, $Li^+$ Dynamics and Applications. *Prog. Mater. Sci.* **2017**, *88*, 325−411.

(8) Thangadurai, V.; Kaack, H.; Weppner, W. Novel Fast Lithium Ion Conduction in Garnet-Type $Li_5La_3M_2O_{12}$ (M = Nb, Ta). *J. Am. Ceram. Soc.* **2003**, *86*, 437−440.

(9) Thangadurai, V.; Narayanan, S.; Pinzaru, D. Garnet-type Solid-State Fast Li Ion Conductors for Li Batteries: Critical Review. *Chem. Soc. Rev.* **2014**, *43*, 4714−4727.

(10) Thangadurai, V.; Adams, S.; Weppner, W. Crystal Structure Revision and Identification of $Li^+$-Ion Migration Pathways in the Garnet-like $Li_5La_3M_2O_{12}$ (M = Nb, Ta) Oxides. *Chem. Mater.* **2004**, *16*, 2998−3006.

(11) Cussen, E. J. The Structure of Lithium Garnets: Cation Disorder and Clustering in a New Family of Fast $Li^+$ Conductors. *Chem. Commun.* **2006**, 412−413.

(12) O'Callaghan, M. P.; Lynham, D. R.; Cussen, E. J.; Chen, G. Z. Structure and Ionic-Transport Properties of Lithium-Containing Garnets $Li_3Ln_3Te_2O_{12}$ (Ln = Y, Pr, Nd, Sm-Lu). *Chem. Mater.* **2006**, *18*, 4681−4689.

(13) Percival, J.; Kendrick, E.; Slater, P. R. Synthesis and Characterisation of the Garnet-Related Li Ion Conductor, $Li_5Nd_3Sb_2O_{12}$. *Mater. Res. Bull.* **2008**, *43*, 765−770.

(14) Percival, J.; Kendrick, E.; Slater, P. R. Synthesis and Conductivities of the Garnet-Related Li Ion Conductors, $Li_5Ln_3Sb_2O_{12}$ (Ln=La, Pr, Nd, Sm, Eu). *Solid State Ionics* **2008**, *179*, 1666−1669.

(15) Thangadurai, V.; Weppner, W. $Li_6ALa_2Ta_2O_{12}$ (A = Sr, Ba): Novel Garnet-Like Oxides for Fast Lithium Ion Conduction. *Adv. Funct. Mater.* **2005**, *15*, 107−112.



DOI: 10.1021/acs.chemmater.9b03526
*Chem. Mater.* 2020, 32, 215−223

(16) Percival, J.; Slater, P. R. Identification of the Li Sites in the Li Ion Conductor, $Li_6SrLa_2Nb_2O_{12}$, through Neutron Powder Diffraction Studies. *Solid State Commun.* **2007**, *142*, 355−357.
(17) Percival, J.; Apperley, D.; Slater, P. R. Synthesis and Structural Characterisation of the Li Ion Conducting Garnet-Related Systems, $Li_6ALa_2Nb_2O_{12}$ (A=Ca, Sr). *Solid State Ionics* **2008**, *179*, 1693−1696.
(18) Buschmann, H.; Dolle, J.; Berendts, S.; Kuhn, A.; Bottke, P.; Wilkening, M.; Heitjans, P.; Senyshyn, A.; Ehrenberg, H.; Lotnyk, A.; Duppel, V.; Kienle, L.; Janek, J. Structure and Dynamics of the Fast Lithium Ion Conductor "$Li_7La_3Zr_2O_{12}$. *Phys. Chem. Chem. Phys.* **2011**, *13*, 19378−19392.
(19) Wolfenstine, J.; Ratchford, J.; Rangasamy, E.; Sakamoto, J.; Allen, J. L. Synthesis and High Li-Ion Conductivity of Ga-Stabilized Cubic $Li_7La_3Zr_2O_{12}$. *Mater. Chem. Phys.* **2012**, *134*, 571−575.
(20) Howard, M. A.; Clemens, O.; Kendrick, E.; Knight, K. S.; Apperley, D. C.; Anderson, P. A.; Slater, P. R. Effect of Ga Incorporation on the Structure and Li Ion Conductivity of $La_3Zr_2Li_7O_{12}$. *Dalton Trans.* **2012**, *41*, 12048−12053.
(21) Adams, S.; Rao, R. P. Ion Transport and Phase Transition in $Li_{7-x}La_3(Zr_{2-x}M_x)O_{12}$ (M = $Ta^{5+}$, $Nb^{5+}$, x = 0, 0.25). *J. Mater. Chem.* **2012**, *22*, 1426−1434.
(22) Howard, M. A.; Clemens, O.; Knight, K. S.; Anderson, P. A.; Hafiz, S.; Panchmatia, P. M.; Slater, P. R. Synthesis, Conductivity and Structural Aspects of $Nd_3Zr_2Li_{7-3x}Al_xO_{12}$. *J. Mater. Chem. A* **2013**, *1*, 14013−14022.
(23) El Shinawi, H.; Janek, J. Stabilization of Cubic Lithium-Stuffed Garnets of the Type "$Li_7La_3Zr_2O_{12}$" by Addition of Gallium. *J. Power Sources* **2013**, *225*, 13−19.
(24) Howard, M. A.; Clemens, O.; Parvathy, A. S.; Anderson, P. A.; Slater, P. R. Synthesis and Ionic Conductivity of New High Li Ion Content Garnets, $LnSr_2Ta_2Li_7O_{12}$ (Ln = La, Pr, Nd, Sm, Gd). *J. Alloys Compd.* **2016**, *670*, 78−84.
(25) Murugan, R.; Thangadurai, V.; Weppner, W. Fast Lithium Ion Conduction in Garnet-Type $Li_7La_3Zr_2O_{12}$. *Angew. Chem., Int. Ed.* **2007**, *46*, 7778−7781.
(26) Awaka, J.; Kijima, N.; Hayakawa, H.; Akimoto, J. Synthesis and Structure Analysis of Tetragonal $Li_7La_3Zr_2O_{12}$ with the Garnet-Related Type Structure. *J. Solid State Chem.* **2009**, *182*, 2046−2052.
(27) Awaka, J.; Kijima, N.; Kataoka, K.; Hayakawa, H.; Ohshima, K.-i.; Akimoto, J. Neutron Powder Diffraction Study of Tetragonal $Li_7La_3Hf_2O_{12}$ with the Garnet-Related Type Structure. *J. Solid State Chem.* **2010**, *183*, 180−185.
(28) O'Callaghan, M. P.; Cussen, E. J. Lithium Dimer Formation in the Li-Conducting Garnets $Li_{5+x}Ba_xLa_{3-x}Ta_2O_{12}$ ($0 < x \leq 1.6$). *Chem. Commun.* **2007**, *20*, 2048−2050.
(29) Cussen, E. J. Structure and Ionic Conductivity in Lithium Garnets. *J. Mater. Chem.* **2010**, *20*, 5167−5173.
(30) Percival, J.; Kendrick, E.; Smith, R. I.; Slater, P. R. Cation Ordering in Li Containing Garnets: Synthesis and Structural Characterisation of the Tetragonal System, $Li_7La_3Sn_2O_{12}$. *Dalton Trans.* **2009**, 5177−5181.
(31) Larraz, G.; Orera, A.; Sanjuán, M. L. Cubic Phases of Garnet-Type $Li_7La_3Zr_2O_{12}$: The Role of Hydration. *J. Mater. Chem. A* **2013**, *1*, 11419−11428.
(32) Geiger, C. A.; Alekseev, E.; Lazic, B.; Fisch, M.; Armbruster, T.; Langner, R.; Fechtelkord, M.; Kim, N.; Pettke, T.; Weppner, W. Crystal Chemistry and Stability of "$Li_7La_3Zr_2O_{12}$" Garnet: A Fast Lithium-Ion Conductor. *Inorg. Chem.* **2011**, *50*, 1089−1097.
(33) Ohta, S.; Kobayashi, T.; Asaoka, T. High Lithium Ionic Conductivity in the Garnet-Type Oxide $Li_{7-x}La_3(Zr_{2-x}, Nb_x)O_{12}$ (x = 0 − 2). *J. Power Sources* **2011**, *196*, 3342−3345.
(34) Kumazaki, S.; Iriyama, Y.; Kim, K.-H.; Murugan, R.; Tanabe, K.; Yamamoto, K.; Hirayama, T.; Ogumi, Z. High Lithium Ion Conductive $Li_7La_3Zr_2O_{12}$ by Inclusion of Both Al and Si. *Electrochem. Commun.* **2011**, *13*, 509−512.
(35) van den Broek, J.; Afyon, S.; Rupp, J. L. M. Interface-Engineered All-Solid-State Li-Ion Batteries Based on Garnet-Type Fast $Li^+$ Conductors. *Adv. Energy Mater.* **2016**, *6*, No. 1600736.
(36) Galven, C.; Fourquet, J.-L.; Crosnier-Lopez, M.-P.; Le Berre, F. Instability of the Lithium Garnet $Li_7La_3Sn_2O_{12}$: $Li^+/H^+$ Exchange and Structural Study. *Chem. Mater.* **2011**, *23*, 1892−1900.
(37) Truong, L.; Howard, M.; Clemens, O.; Knight, K. S.; Slater, P. R.; Thangadurai, V. Facile Proton Conduction in $H^+/Li^+$ Ion-Exchanged Garnet-Type Fast Li-Ion Conducting $Li_5La_3Nb_2O_{12}$. *J. Mater. Chem. A* **2013**, *1*, 13469−13475.
(38) Brugge, R. H.; Hekselman, A. K. O.; Cavallaro, A.; Pesci, F. M.; Chater, R. J.; Kilner, J. A.; Aguadero, A. Garnet Electrolytes for Solid State Batteries: Visualization of Moisture-Induced Chemical Degradation and Revealing Its Impact on the Li-Ion Dynamics. *Chem. Mater.* **2018**, *30*, 3704−3713.
(39) Cheng, L.; Crumlin, E. J.; Chen, W.; Qiao, R.; Hou, H.; Franz Lux, S.; Zorba, V.; Russo, R.; Kostecki, R.; Liu, Z.; Persson, K.; Yang, W.; Cabana, J.; Richardson, T.; Chen, G.; Doeff, M. The Origin of High Electrolyte-Electrode Interfacial Resistances in Lithium Cells Containing Garnet Type Solid Electrolytes. *Phys. Chem. Chem. Phys.* **2014**, *16*, 18294−18300.
(40) Li, Y.; Chen, X.; Dolocan, A.; Cui, Z.; Xin, S.; Xue, L.; Xu, H.; Park, K.; Goodenough, J. B. Garnet Electrolyte with an Ultralow Interfacial Resistance for Li-Metal Batteries. *J. Am. Chem. Soc.* **2018**, *140*, 6448−6455.
(41) Kotobuki, M.; Munakata, H.; Kanamura, K.; Sato, Y.; Yoshidab, T. Compatibility of $Li_7La_3Zr_2O_{12}$ Solid Electrolyte to All-Solid-State Battery Using Li Metal Anode. *J. Electrochem. Soc.* **2010**, *157*, A1076−A1079.
(42) Sudo, R.; Nakata, Y.; Ishiguro, K.; Matsui, M.; Hirano, A.; Takeda, Y.; Yamamoto, O.; Imanishi, N. Interface Behavior between Garnet-Type Lithium-Conducting Solid Electrolyte and Lithium Metal. *Solid State Ionics* **2014**, *262*, 151−154.
(43) Sharafi, A.; Meyer, H. M.; Nanda, J.; Wolfenstine, J.; Sakamoto, J. Characterizing the Li−$Li_7La_3Zr_2O_{12}$ Interface Stability and Kinetics as a Function of Temperature and Current Density. *J. Power Sources* **2016**, *302*, 135−139.
(44) Fu, K.; Gong, Y.; Hitz, G. T.; McOwen, D. W.; Li, Y.; Xu, S.; Wen, Y.; Zhang, L.; Wang, C.; Pastel, G.; Dai, J.; Liu, B.; Xie, H.; Yao, Y.; Wachsman, E. D.; Hu, L. Three-Dimensional Bilayer Garnet Solid Electrolyte Based High Energy Density Lithium Metal−Sulfur Batteries. *Energy Environ. Sci.* **2017**, *10*, 1568−1575.
(45) Luo, W.; Gong, Y.; Zhu, Y.; Li, Y.; Yao, Y.; Zhang, Y.; Fu, K. K.; Pastel, G.; Lin, C. F.; Mo, Y.; Wachsman, E. D.; Hu, L. Reducing Interfacial Resistance between Garnet-Structured Solid-State Electrolyte and Li-Metal Anode by a Germanium Layer. *Adv. Mater.* **2017**, *29*, No. 1606042.
(46) Wang, C.; Gong, Y.; Liu, B.; Fu, K.; Yao, Y.; Hitz, E.; Li, Y.; Dai, J.; Xu, S.; Luo, W.; Wachsman, E. D.; Hu, L. Conformal, Nanoscale ZnO Surface Modification of Garnet-Based Solid-State Electrolyte for Lithium Metal Anodes. *Nano Lett.* **2017**, *17*, 565−571.
(47) Dai, J.; Yang, C.; Wang, C.; Pastel, G.; Hu, L. Interface Engineering for Garnet-Based Solid-State Lithium-Metal Batteries: Materials, Structures, and Characterization. *Adv. Mater.* **2018**, *30*, No. 1802068.
(48) Han, X.; Gong, Y.; Fu, K. K.; He, X.; Hitz, G. T.; Dai, J.; Pearse, A.; Liu, B.; Wang, H.; Rubloff, G.; Mo, Y.; Thangadurai, V.; Wachsman, E. D.; Hu, L. Negating Interfacial Impedance in Garnet-Based Solid-State Li Metal Batteries. *Nat. Mater.* **2017**, *16*, 572−579.
(49) Yoshima, K.; Harada, Y.; Takami, N. Thin Hybrid Electrolyte Based on Garnet-Type Lithium-Ion Conductor $Li_7La_3Zr_2O_{12}$ for 12 V-Class Bipolar Batteries. *J. Power Sources* **2016**, *302*, 283−290.
(50) Rangasamy, E.; Wolfenstine, J.; Allen, J.; Sakamoto, J. The Effect of 24c-Site (A) Cation Substitution on the Tetragonal−Cubic Phase Transition in $Li_{7-x}La_{3-x}A_xZr_2O_{12}$ Garnet-Based Ceramic Electrolyte. *J. Power Sources* **2013**, *230*, 261−266.
(51) Toby, B. H. EXPGUI, a Graphical User Interface for GSAS. *J. Appl. Crystallogr.* **2001**, *34*, 210−213.
(52) Kresse, G.; Hafner, J. Ab Initio Molecular-Dynamics Simulation of the Liquid-Metal-Amorphous-Semiconductor Transition in Germanium. *Phys. Rev. B: Condens. Matter.* **1994**, *49*, 14251−14269.


DOI: 10.1021/acs.chemmater.9b03526
*Chem. Mater.* 2020, 32, 215−223

(53) Blöchl, P. E. Projector Augmented-Wave Method. *Phys. Rev. B: Condens. Matter.* **1994**, *50*, 17953−17979.
(54) Perdew, J. P.; Ruzsinszky, A.; Csonka, G. I.; Vydrov, O. A.; Scuseria, G. E.; Constantin, L. A.; Zhou, X.; Burke, K. Restoring the Density-Gradient Expansion for Exchange in Solids and Surfaces. *Phys. Rev. Lett.* **2008**, *100*, No. 136406.
(55) Krukau, A. V.; Vydrov, O. A.; Izmaylov, A. F.; Scuseria, G. E. Influence of the Exchange Screening Parameter on the Performance of Screened Hybrid Functionals. *J. Chem. Phys.* **2006**, *125*, No. 224106.
(56) Irvine, J. T. S.; Sinclair, D. C.; West, A. R. Electroceramics: Characterization by Impedance Spectroscopy. *Adv. Mater.* **1990**, *2*, 132−138.
(57) Dong, B.; Jarkaneh, R.; Hull, S.; Reeves-McLaren, N.; Biendicho, J. J.; West, A. R. Synthesis, Structure and Electrical Properties of N-doped $Li_3VO_4$. *J. Mater. Chem. A* **2016**, *4*, 1408−1413.
(58) Dong, B.; Yan, J.; Walkley, B.; Inglis, K. K.; Blanc, F.; Hull, S.; West, A. R. Synthesis and Characterisation of the New Oxyfluoride $Li^+$ Ion Conductor, $Li_5SiO_4F$. *Solid State Ionics* **2018**, *327*, 64−70.
(59) Trofimov, A. A.; Li, C.; Brinkman, K. S.; Jacobsohn, L. G. Luminescence Investigation of Ce Incorporation in Garnet-Type $Li_7La_3Zr_2O_{12}$. *Opt. Mater.* **2017**, *68*, 7−10.
(60) Kendrick, E.; Knight, K. S.; Slater, P. R. Ambi-Site Substitution of Mn in Lanthanum Germanate Apatites. *Mater. Res. Bull.* **2009**, *44*, 1806−1809.
(61) Yeandel, S. R.; Chapman, B. J.; Slater, P. R.; Goddard, P. Structure and Lithium-Ion Dynamics in Fluoride-Doped Cubic $Li_7La_3Zr_2O_{12}$ (LLZO) Garnet for Li Solid-State Battery Applications. *J. Phys. Chem. C* **2018**, *122*, 27811−27819.


DOI: 10.1021/acs.chemmater.9b03526
*Chem. Mater.* 2020, 32, 215−223